Polar Geosci., **12**, 227–239, 1999

A CASE STUDY OF GENERATING A DIGITAL ELEVATION MODEL FOR THE SÔYA COAST AREA, ANTARCTICA, USING JERS-1 SAR INTERFEROMETRY

Taku OZAWA[1], Koichiro DOI[2] and Kazuo SHIBUYA[2]

[1]*Department of Polar Science, School of Mathematical and Physical Sciences, The Graduate University for Advanced Studies, Kaga 1-chome, Itabashi-ku, Tokyo 173-8515*
[2]*National Institute of Polar Research, Kaga 1-chome, Itabashi-ku, Tokyo 173-8515*

Abstract: The three-pass synthetic aperture radar (SAR) interferometry method has been applied to three time-serial scenes (two SAR pairs) over the Sôya Coast area, Antarctica, observed by the Japanese Earth Resources Satellite 1 (JERS-1). For simplicity, we assumed that the ice flow during 88 days (2 repeat periods of JERS-1) was constant. Interferometric fringes associated with ice flow/deformation were removed using the two SAR pairs to leave the topographic fringes. The resultant topographic fringes were converted to the relative surface elevations above sea level. There are 23 suitable ground control points (GCPs) in the region concerned, covering the height range from 0 to 600 m. A digital elevation model (DEM) was created in order that the model heights fit the GCP heights in a least squares sense. The obtained DEM grids with a spatial resolution of 50 m by 50 m have a root-mean-square (rms) error of 15.3 m. As for the GTOPO30 model grids with a 30 arc-second resolution in the same region, similar comparison of the model heights with the GCP heights resulted in a bias of –66.2 m and rms error of 131.7 m, which is worse than the SAR derived DEM by one order of magnitude. It is also noted that 12 GCPs on the islands and coastal outcropped areas are incorrectly located outside of the land area when mapped in the GTOPO30 contours. In spite of several remaining problems to be solved, SAR interferometry can effectively be applied to generate DEMs on the vast inaccessible ice sheet of Antarctica.

key words: SAR, interferometry, DEM, JERS-1, Sôya-Coast

1. Introduction

More than 97% of the Antarctic continent is covered by a vast ice sheet. The topographic mapping of the Antarctic ice sheet is important for geophysical and glaciological studies in Antarctica. Topographic maps have been made by aerial photogrammetry, combined with the results of ground geodetic surveying data. However, application of this method in the Antarctic region is limited to local areas around coastal outcrops. Although height on the ice sheet has been measured by using satellite Doppler positioning receivers (*e.g.* SHIBUYA and ITO, 1983), or recently by using Global Positioning System (GPS) receivers (*e.g.* OOTAKI and FUJIWARA, 1998), utilization of these satellite receivers is still limited to local/regional areas by inaccessibility and/or insufficient time in the field for the vast number of ground data required for topographic mapping of the ice sheet.

The United States Geological Survey (USGS) has prepared a global digital elevation model (DEM) named GTOPO30 with 30 arc-second gridding in both latitudinal and longitudinal directions and 1 m height resolution (USGS, 1996). In Antarctica, GTOPO30 is based on the Antarctic Digital Database (ADD; BRITISH ANTARCTIC SURVEY *et al.*, 1993) compiled by the Scientific Committee on Antarctic Research (SCAR) Working Group on Geodesy and Geographic Information (WGGGI). GTOPO30 documentation (USGS, 1996) describes the vertical accuracy of ADD as "highly variable" and does not give an error estimate for height, in spite of the rather good 1 m resolution. If a more accurate DEM of the Antarctic ice sheet surface than ADD can observably be obtained within the short time-span of one month, repeatedly obtained DEMs may provide information on the ice dynamics related to the mass balance of Antarctica.

Synthetic aperture radar (SAR) is an active microwave remote sensing tool which is installed on an aircraft or satellite to detect backscattering properties of return pulses from ground. SAR interferometry utilizes return pulse phases. It has successfully been applied to generate surface topography of land with an accuracy of 2–10 m using an L-band SAR sensor on an aircraft (ZEBKER and GOLDSTEIN, 1986). SAR interferometry has also been applied to detect surface deformations associated with the Landers Earthquake with an accuracy of around 3 cm (MASSONET *et al.*, 1993). Thus the SAR interferometry technique enables us to determine detailed surface topography and displacement over a wide area. Moreover this technique doesn't depend on weather, because the microwaves penetrate clouds. However, the SAR interferometry technique is not always applicable, because rapid change of surface dielectricity and fast movement of the target cause change of backscatter characteristics and result in loss of coherence for interferometry.

The processing technique for SAR interferometry has been improved year after year, and SAR interferometry has become a powerful tool for studies of Antarctic ice sheet dynamics. For example, GOLDSTEIN *et al.* (1993) demonstrated detection of ice flow in the Rutford Ice Stream region. Several studies have been made to detect the grounding line of the ice sheet and ice shelf motion due to the ocean tide (*e.g.* DIETRICH *et al.*, 1997; MÜLLER *et al.*, 1997; RIGNOT and MACAYEAL, 1998). The study areas in the above references are summarized in Fig. 1a.

The above studies are based on SAR scenes observed by the C-band (5.7 cm wavelength) sensor on the European Remote Sensing Satellite 1 (ERS-1) which was launched in July 1991 by the European Space Agency (ESA) for the 3-day repeat period (ice phase). As compared with C-band SAR, few attempts have been made to conduct antarctic ice studies using L-band (23.5 cm wavelength) SAR on the Japanese Earth Resources Satellite 1 (JERS-1), which was launched in November 1992 by the National Space Development Agency of Japan (NASDA). Only two trials of DEM generation were conducted on the outcropped area of the Amundsen Bay region (DOI *et al.*, 1998), and on the ice sheet area around the Yamato Mountains region (KIMURA *et al.*, 1999) in East Antarctica (see also Fig. 1a).

Because scattering properties of ice/snow may not change for a longer duration for the L-band wavelength as compared with the C-band wavelength, SAR interferometry may adequately be applied to the JERS-1 scenes observed by longer duration (repeat cycle 44 days) than ERS-1 scenes observed by shorter duration (repeat cycle 3 days).

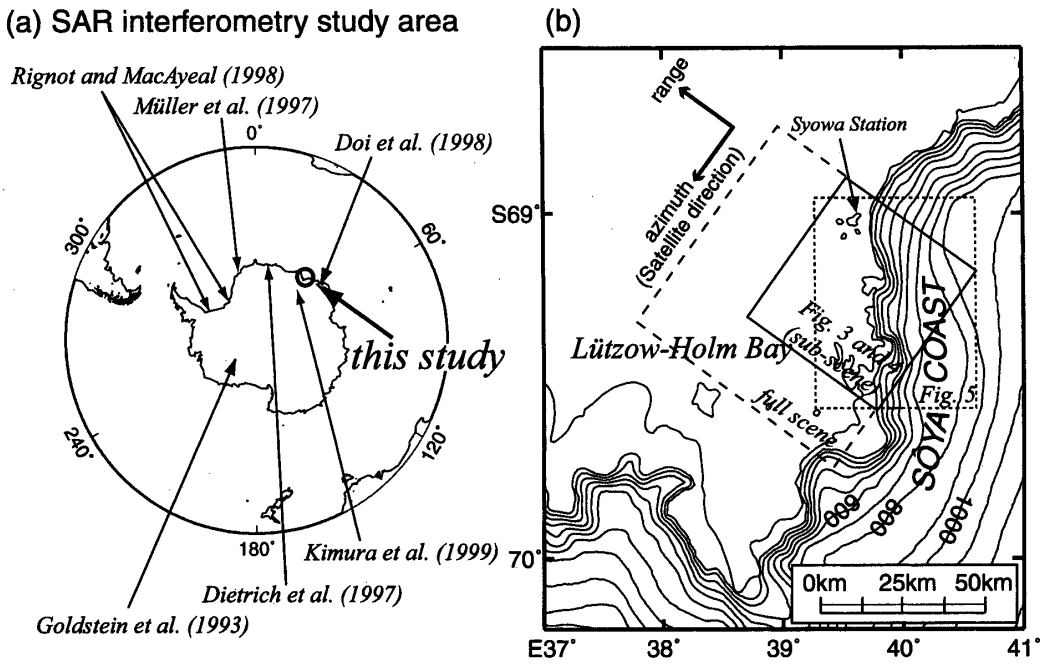

Fig. 1. (a) Location of the Sôya Coast area (this study area indicated by a thick open circle) and other research areas using SAR interferometry in Antarctica. (b) Schematic map in the Sôya Coast region. Contours at intervals of 100 m are drawn from the GTOPO30 topographic database (USGS, 1996). Seacoast is drawn from the coastline data included in the Generic Mapping Tools (GMT) package (WESSEL and SMITH, 1995). Dashed box coincides with the observed SAR full scene area, while solid box indicates the area analyzed in this study which is called the sub-scene area (see also Figs. 3 and 4). A DEM within the dotted box (Fig. 5) was generated in this study.

JERS-1 SAR interferometry may also reveal backscattering characteristics from the ice sheet surface which were not found by C-band SAR interferometry. We analyzed three time-serial JERS-1 SAR scenes over the Sôya Coast area (see Fig. 1b) to see if an appropriate DEM over the ice sheet can be obtained.

2. Theoretical Background of SAR Interferometry

The detailed principle of SAR interferometry for topographic mapping has been described in many articles (*e.g.* GRAHAM, 1974; ZEBKER and GOLDSTEIN, 1986; LI and GOLDSTEIN, 1990; URAI and YAMAGUCHI, 1996). We briefly summarize causes of interferometric fringes in the case of a satellite repeat-pass for our case study below.

Figure 2 indicates schematically the observational geometry of SAR interferometry. There is a phase change component ϕ_{orb} which comes from the geometry of platforms (hereafter referred to as orbital fringe). The orbital fringe can be described by

$$\phi_{orb} = 4\pi B \sin(\theta - \alpha) / \lambda, \quad (1)$$

where B is the distance between the two satellite positions (baseline length), θ is the look angle, α is the angle of the baseline with respect to a horizontal surface, and λ is the radar pulse wavelength.

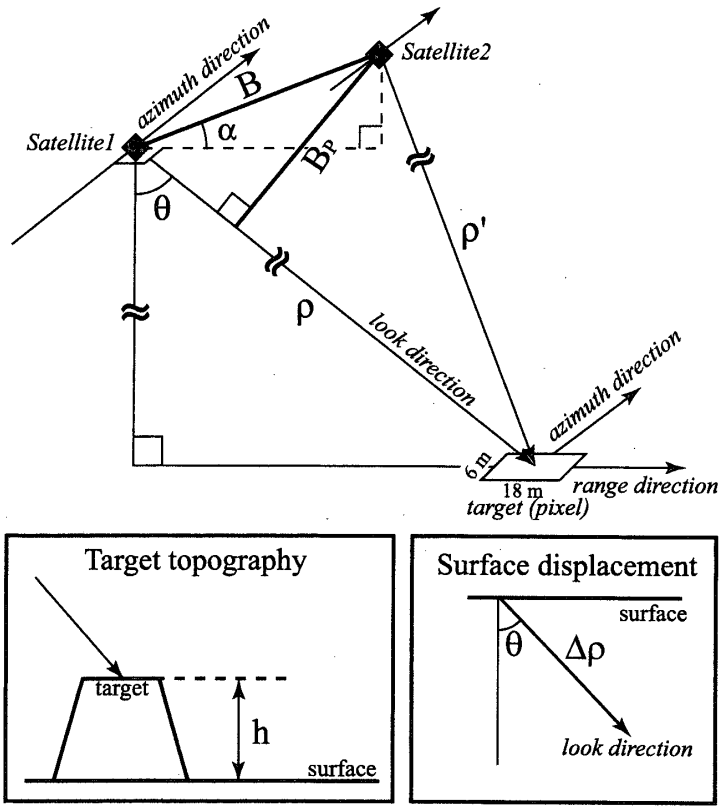

Fig. 2. Schematic observational geometry of the SAR interferometry. B is the distance between the two satellite positions (baseline length), B_P is the perpendicular component of the baseline length relative to the look direction, θ is the look angle (off nadir angle), α is the angle of the baseline with respect to a horizontal surface, ρ and ρ' are the distances between the satellite and the target pixel, h is the topographic height of the target and Δρ is the slant range change which resulted from the surface deformation.

There is also a phase change component which comes from surface topography (hereafter referred to as topographic fringe). The related phase change ϕ_{topo} can be expressed as

$$\phi_{topo} = 4\pi h B_P/\lambda\rho \sin\theta, \tag{2}$$

with

$$B_P = B \cos(\theta - \alpha), \tag{2}'$$

where ρ is the distance between the satellite and the target point (slant range), h is the topographic height of the target, and B_P is the vertical component of the baseline length relative to the look direction.

There is another phase change component caused by surface displacement (hereafter referred to as displacement fringe). The associated phase change ϕ_{disp} is:

$$\phi_{disp} = -4\pi\Delta\rho/\lambda, \tag{3}$$

where $\Delta\rho$ is the slant range change which results from the surface deformation.

Then the observed phase difference will be the summation of the above three fringe

components (1), (2) and (3) plus noise:

$$\phi_{\text{total}} = \phi_{\text{orb}} + \phi_{\text{topo}} + \phi_{\text{disp}} + \text{noise}. \quad (4)$$

From eqs. (1)–(3), it is clear that the orbital and topographic fringes are dependent on the baseline component, while the displacement fringe is independent. Because the recorded phase differences are within the range of $-\pi$~$+\pi$, the recovered slant range ρ may have ambiguity of integer multiples of 2π. The true phase difference can be determined by resolving this ambiguity after *e.g.* GOLDSTEIN *et al.* (1988).

3. Data Analysis

3.1. Pre-interferogram processing

The JERS-1 SAR data sets used in this study were obtained from observations on June 16 (first scene), July 30 (second scene) and September 12 (third scene) in 1996 at a time-interval of 44 days. These data were downlinked to the Alaska SAR Facility (ASF), Fairbanks, Alaska. The above observed SAR data sets covered a 75 km×75 km rectangular area around the Sôya Coast (Path-Row number 187–418 defined by NASDA) that included the Japanese Antarctic Station Syowa (full scene in Fig. 1b indicated by the dashed rectangle). We analyzed the 45 km×55 km sub-scene area shown by the solid rectangle. The SAR scene consists of the single look complex (SLC) pixels which have spatial resolution of 18 m in the range direction and 6 m in the azimuth direction, respectively (see Fig. 2). As there are 23 ground control points (GCPs) which were positioned by triangulation, trilateration, satellite Doppler or GPS positioning, this sub-scene indicated in Fig. 1b will give us a good test field for SAR interferometry.

Downlinked SAR data were converted into the CEOS (Committee on Earth Observation Satellite) formatted raw data by NASDA/EOC (Earth Observation Center). From the CEOS formatted raw data, we generated SLCs over each scene, where phase and magnitude of backscatter radar pulse from each target (pixel) in the full scene area were expressed by a single complex number. Location and scale of one SLC were correlated with those of the other SLC after affine transformation. Then, phases from the same pixel of the corresponding SLCs that gave the best coherence were obtained. The phase differences of the best correlated phases will have systematic features corresponding to the above three components, and characteristic fringes will appear in the interferometric image. Then we generated interferogram pairs from the first and second SAR scenes (hereafter named the first pair), and from the second and third SAR scenes (hereafter named the second pair), using the Vexcel 3DSAR SAR processing system Version 2.0 (VEXCEL CORPORATION, 1998).

In order to deduce topographic fringes, the orbital fringes by eq. (1) must be reduced adequately. In general, the orbital fringes can be removed using orbital information, because the baseline component in eq. (1) can be estimated from the known satellite coordinates. However, unlike ERS-1, there are few satellite tracking stations for JERS-1 over the world, and the JERS-1 orbit determination seems inaccurate to 100 m, especially in the Antarctic region. Even when the satellite baseline is not known accurately, as is the case for the JERS-1 orbits, it is noted that the orbit fringe is linear in the azimuthal direction and similar to a quadratic curve in the range direction; TOBITA *et al.* (1998)

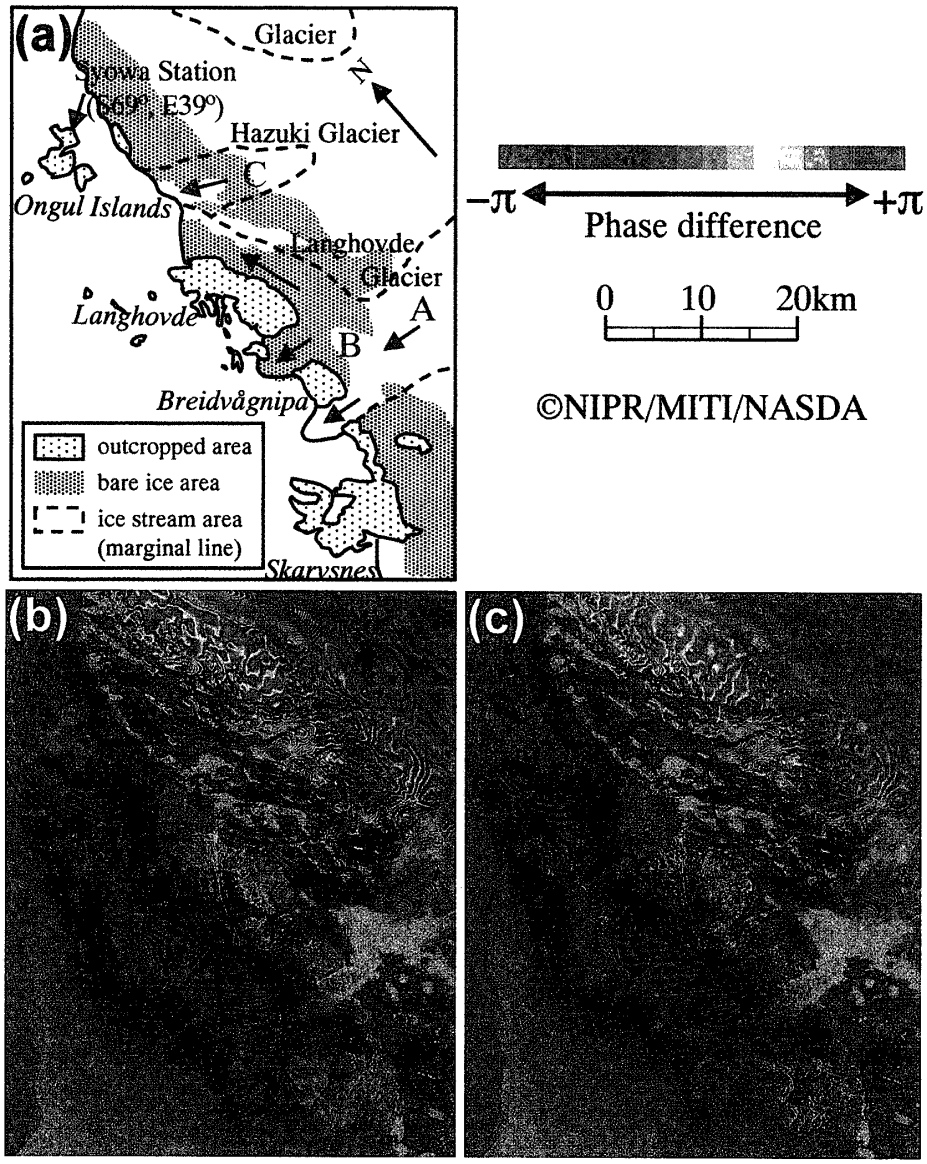

Fig. 3. *(a) Surface conditions of radar pulse backscattering in the study area. They are basically grouped into two regions, outcropped regions (dotted region) and an ice sheet region. The ice sheet region includes bare ice areas (shaded area) and ice streams. The solid line indicates the coastline and the dashed lines indicate boundaries of the ice streams. The red arrows indicate schematic ice flow directions of the ice streams. (b) The first-pair interferogram superimposed on the monochromatic intensity image derived from the JERS-1 SAR observed scenes on June 16 (first scene) and July 30 (second scene) in 1996. The backscatter intensity is gray-scaled so that the strongest backscatter is white and the weakest one is black. (c) The second-pair interferogram derived from the scenes on July 30 and September 12 (third scene). The color bars in Figs. 3b and 3c indicate the phase difference from $-\pi$ to $+\pi$.*

called it "Kamaboko" shaped.

TOBITA *et al.* (1998) then developed a dedicated method to empirically model this semi-cylindrical function, and we followed their procedure to reduce the orbit fringes. In order to further suppress the effect of satellite baseline uncertainty, we constrained the

slant ranges so that all observed backscatter phases from the seacoast line surrounding outcropped areas such as Langhovde and Skarvsnes in Fig. 3a gave the same 0 m height.

3.2. Surface conditions of the research area and two-pass interferogram

Figure 3a shows schematically the surface conditions in the research area. There are four major outcropped areas (dotted area): the Ongul Islands, Langhovde, Breidvågnipa and Skarvsnes. Adjacent to the outcropped areas along the coast, there are bare ice areas (shaded areas in Fig. 3a) characterized by slow ice motion (~5 m/year by SHIMIZU *et al.*, 1975) and/or surface melting during the summer season. These areas appear blue in the aerial photographs. Toward higher elevation to the upper-right in Fig. 3a, the bare ice area is replaced by the snow cover area. The ice sheet area in this research area includes two major ice streams, Hazuki Glacier and Langhovde Glacier. The ice flow directions in these ice streams are illustrated by red arrows in Fig. 3a.

Monochromatic SAR images in Figs. 3b and 3c show backscatter intensity distributions. Because of lower dielectricity and more rugged surface than over the ice sheet, outcropped areas are usually characterized by strong backscatter intensities, and appear "white". Many shears and rough undulations within the ice stream areas are also characterized by strong backscatter intensities, highlighting flowlines as indicated by GOLDSTEIN *et al.* (1993). Bare ice areas, on the contrary, appear "black". This weak backscattering may be due to total reflection of radar pulses at the smooth ice surface, as indicated by TAKAHASHI *et al.* (1995).

The color bands superposed onto the monochromatic SAR intensity images in Figs. 3b and 3c show interferograms of the first pair and the second pair, respectively, which were corrected for the orbital fringe components described in Section 3.1. The color legend from blue through pink to blue indicates a 2π change of the phase difference. The fringes clearly appeared on all outcropped areas, on most of the ice sheet areas and on the higher part (around A in Fig. 3a) of the ice streams.

The ice streams (around A and C in Fig. 3a) were basically characterized by denser fringe bands over the marginal areas than those over the central flowlines; this is consistent with larger velocity gradients around the marginal portion of the ice streams along the transverse direction (marginal shear zone: see GOLDSTEIN *et al.*, 1993). The lower part (around B in Fig. 3a) of the ice streams did not show fringes; this must be related to loss of coherence associated with too fast a movement of the pixels. Insignificant interferograms on the bare ice area must be related to decorrelation by weak backscattering radar pulses. In our interferogram pairs, B_P values calculated from orbit information were 41 m for the first pair and 957 m for the second pair; these values are within the empirical range of 0–1000 m for good coherence.

3.3. Three pass method for extracting topographic fringes

KWOK and FAHNESTOCK (1996) and JOUGHIN *et al.* (1996) removed the effect of ice flow by using time-serial three-passes (scenes) over the same region, and obtained topographic maps of the ice sheet over Greenland with a relative accuracy of 2–3 m (hereafter we call this the three-pass method).

After removing orbital fringes, the fringes on the first and second pairs can be described by

$$\phi_{\text{total},1} = \phi_{\text{topo},1} + \phi_{\text{disp},1} + \text{noise}_1,$$
$$\phi_{\text{total},2} = \phi_{\text{topo},2} + \phi_{\text{disp},2} + \text{noise}_2, \tag{5}$$

where suffixes 1 and 2 indicate remaining fringe components and noise in the first and the second pairs, respectively. If the ice sheet flow velocity is constant and uniform, and if the observation intervals are identical,

$$\phi_{\text{disp},1} = \phi_{\text{disp},2}, \tag{6}$$

can be obtained from eq. (3). Then the three-pass method gives us

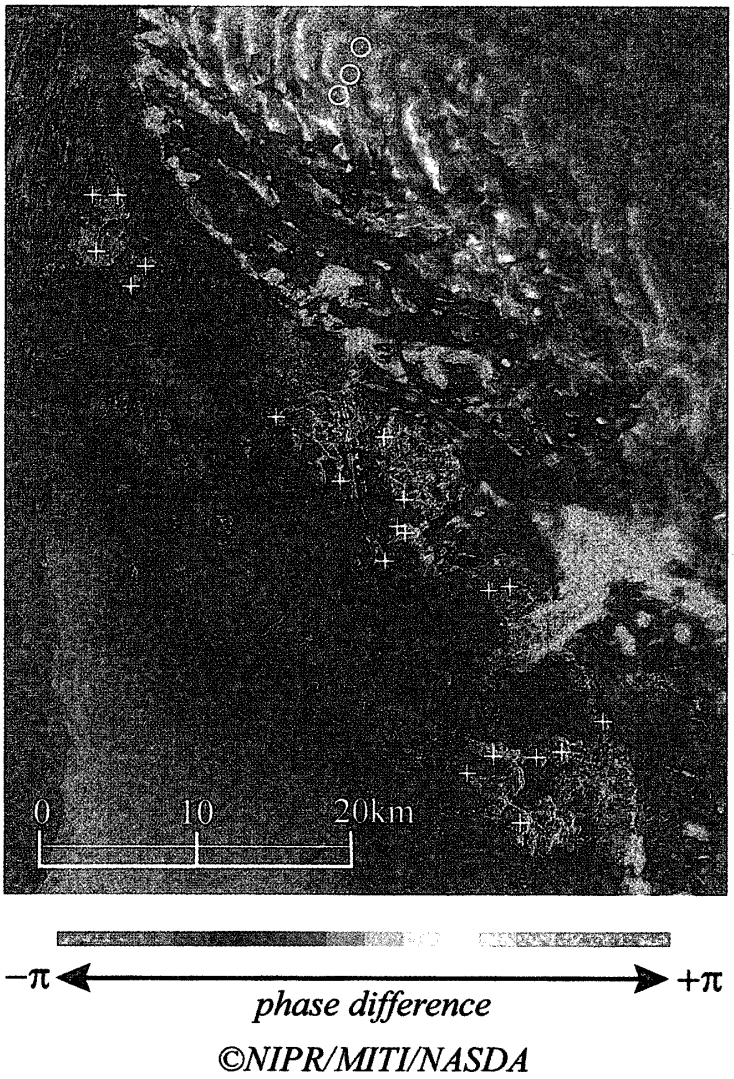

Fig. 4. Three-pass interferogram. The extracted topographic fringes can be seen on the ice sheet and the outcropped areas. Although fringes also appeared on the sea ice area, they are not topographic fringes and not discussed here. The color bar indicates the phase difference from $-\pi$ to $+\pi$, corresponding to the height change of 62 m. White crosses are GCPs on the outcropped area positioned from the Japanese 1:250000 scale maps of Lützow-Holm Bay and the Prince Olav Coast, and open circles are GCPs on the ice sheet which were determined by the GPS survey (KAMIYAMA et al., 1994).

$$\phi_{\text{three-pass}} = \phi_{\text{total},1} - \phi_{\text{total},2} = \phi_{\text{topo},1} - \phi_{\text{topo},2} + \text{noise}, \quad (7)$$

where $\phi_{\text{three-pass}}$ indicates the phase of the three-pass interferogram. It is noted from eq. (2) that the three-pass interferogram phase can be related to the difference of the corresponding B_P values for the first and second pairs.

Figure 4 shows the derived topographic fringes from the two pairs of JERS-1 interferograms by applying the three pass method. It is noted that dense fringe bands along the boundary of the Hazuki and Langhovde Glaciers, mentioned in Section 3.2, disappeared because these features in Figs. 3b and 3c are basically dominated by common shear deformations. Although KWOK and FAHNESTOCK (1996) used ERS-1 ice phase (3-day repeat cycle) SAR data, our JERS-1 SAR data were obtained from the 44-day repeat period. Thus the obtained topographic interferogram in Fig. 4 may still involve an uncancelled displacement fringe component due to possible irregular ice flow during a comparatively long time span of 88 days.

Table 1. Comaprison of the SAR derived model heights and GTOPO30 model heights with the GCP heights.

1	2	3	4	5	6	7
Longitude [deg.]	Latitude [deg.]	GCP height [m]	GTOPO30 height [m]	Residual [m] (GTOPO30 – GCP)	SAR observed height [m]	Residual [m] (Obs. – GCP)
39.61588	-69.00456	22.0	22.0	0.0	21.2	-0.8
39.54645	-69.06012	22.0	22.0	0.0	22.5	0.5
39.62033	-69.17978	22.0	22.0	0.0	25.7	3.7
39.65873	-69.23903	22.0	22.0	0.0	34.2	12.2
39.72942	-69.27178	22.0	27.2	5.2	41.1	19.1
39.64244	-69.29964	22.0	22.0	0.0	31.9	9.9
39.69132	-69.28228	22.0	23.9	1.9	30.1	8.1
39.76983	-69.35600	22.0	104.6	82.6	8.0	-14.0
39.67548	-69.45569	22.0	22.0	0.0	11.3	-10.7
39.56136	-69.44110	22.0	22.0	0.0	5.3	-16.7
39.57464	-68.99507	53.7	22.0	-31.7	44.6	-9.1
39.52337	-69.02547	59.7	22.0	-37.7	56.2	-3.5
39.58691	-69.05176	68.0	22.0	-46.0	50.2	-17.8
39.76349	-69.23022	375.0	98.8	-276.2	382.9	7.9
39.70666	-69.29140	253.0	31.3	-221.7	261.5	8.5
39.79555	-69.35816	338.0	190.9	-147.1	317.5	-20.5
39.81526	-69.46377	245.0	231.6	-13.4	247.5	2.5
39.71030	-69.46233	250.0	26.6	-223.4	257.4	7.4
39.58830	-69.48103	239.0	22.0	-217.0	244.8	5.8
39.58304	-69.47970	400.4	22.0	-378.4	450.0	49.6
40.04802	-69.03458	589.0*	575.2	-13.8	577.6	-11.4
40.08169	-69.02637	606.0*	607.4	1.4	591.9	-14.1
40.10847	-69.01642	631.0*	622.8	-8.2	614.6	-16.4
			mean [m]	-66.1	mean [m]	0.0
			rms [m]	131.7	rms [m]	15.3

columns 1 and 2: Location is expressed by the geodetic coordinates on the GRS80 ellipsoid.
column 3: Star indicates GPS positioning height on the ice sheet by KAMIYAMA et al. (1994), and converted to the GRS80 ellipsoidal height.
column 4: Interpolated from the 3 GTOPO30 model grids surrounding the GCP location. See also inset of Fig. 5a.

4. GTOPO30 and Ground Control Points Around the Sôya Coast

GTOPO30 charts around the Sôya Coast (SR 37-38/1, 3, 5, 6, 9, 10) are based on the Japanese 1:250000 scale maps of Lützow-Holm Bay and the Prince Olav Coast published by the Geographical Survey Institute of Japan. Although the temporal and spatial distribution of the obtained ground control points (GCPs) is not enough to estimate accurate surface topography/flow of the ice sheet, GTOPO30 can be considered to be the most accurate DEM in the region until now.

Table 1 shows the list of the 23 GCPs in the research area, where columns 1 and 2 indicate position coordinates. Since the geoid height in the research area can be estimat-

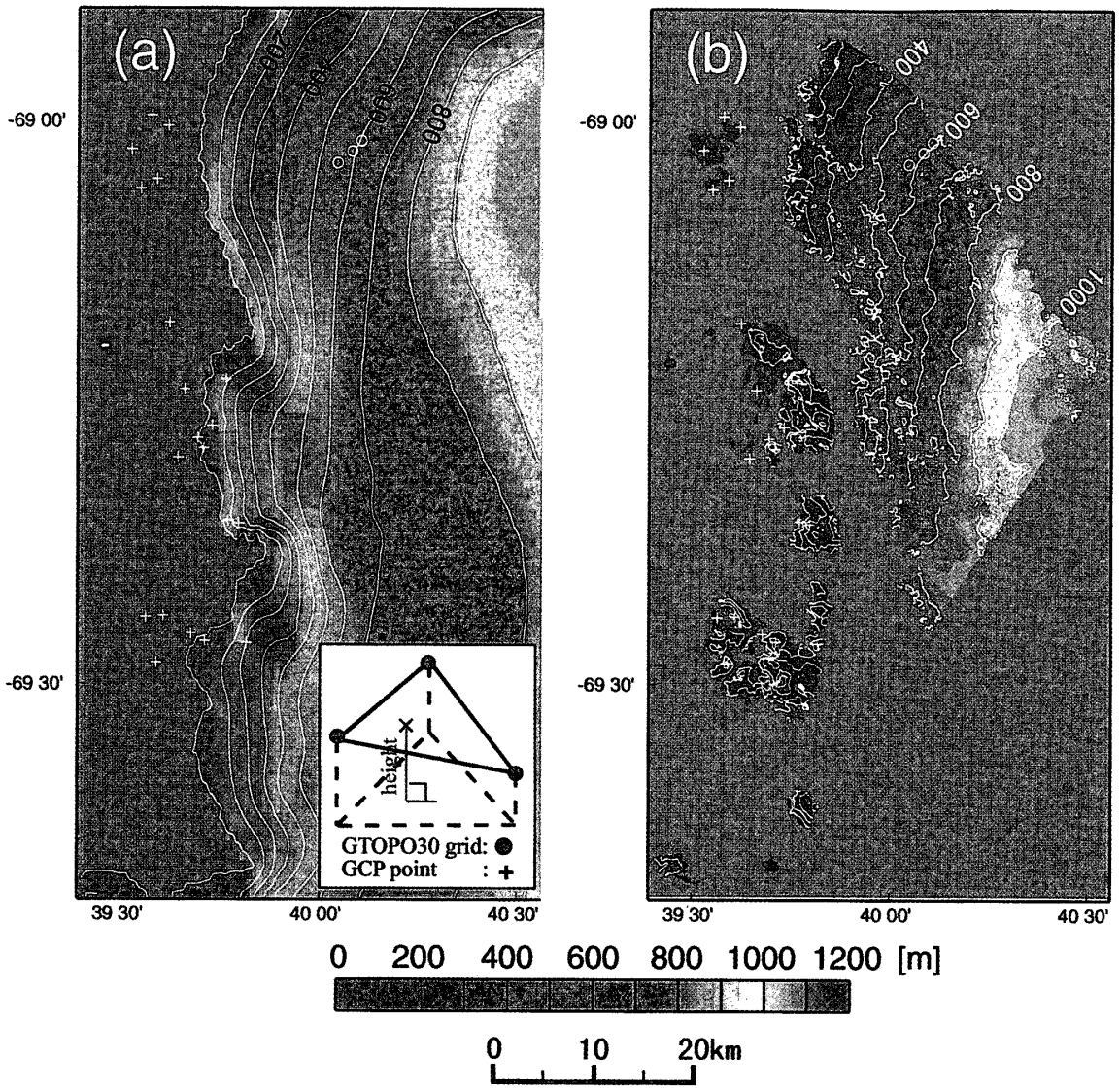

Fig. 5. (a) GTOPO30 terrain model in the Sôya Coast area. A triangular surface element in the lower inset indicates geometry for the estimation of the GCP height from the three nearest GTOPO30 model grid heights. (b) The DEM derived from the three-pass SAR interferometry method. The color bar indicates topographic heights. Contour lines are at intervals of 100 m.

ed as 22 m on the GRS80 ellipsoid considering *e.g.* SHIBUYA *et al.* (1999), the elevations above sea level of the GCPs were converted to ellipsoidal heights as tabulated in column 3. The 20 GCPs out of 23 are somewhat concentrated on the coastal outcropped area (crosses in Fig. 4); only three surveyed points are located on the ice sheet (open circles in Fig. 4 and stars in column 3 of Table 1: KAMIYAMA *et al.*, 1994). The GCPs cover the height range from 0 to 630 m adequately, and their height accuracy is considered to be 1 m for each point on the outcropped area and 2–4 m on the ice sheet.

Figure 5a illustrates the color image of GTOPO30 around the Sôya Coast, where the grids have spatial resolution of 1 km in the latitudinal direction, 0.3 km in the longitudinal direction, and 1 m vertically, respectively. It is noted that GTOPO30 cannot display outcropped areas such as the Ongul Islands and Langhovde. The 12 GCPs among 23 (see crosses in Fig. 5a) are incorrectly located outside of the land area on the GTOPO30 contours.

The GTOPO30 model height at GCP was interpolated from the three nearest grid points by assuming that the ice sheet surface is locally flat (see triangular element in the lower inset of Fig. 5a), and it was listed in column 4 after conversion to the ellipsoidal height. As shown in column 5, the residuals of the GTOPO30 model heights from the GCP heights have an average bias of –66.1 m and a root-mean-square (rms) error of 131.7 m.

5. Comparison of the SAR Interferometry Derived DEM with GCP

Since the SAR range-azimuth coordinate system is rotated against the geodetic coordinate system (see Fig. 1b), the topographic interferogram (Fig. 4) must be adjusted to fit to the north-south direction. Two pixels from clear landmarks were chosen from the Ongul Islands and from Skarvsnes, and such rotation was done so that the baseline connecting the two pixels became superposed onto the same landmarks on the 1:250,000 scale map of Lützow-Holm Bay.

In order to generate a DEM from the topographic interferogram of Fig. 4, the obtained phase differences must be unwrapped correctly (*e.g.* GOLDSTEIN *et al.*, 1988). However, exact phase unwrapping is rather difficult, because there are many discontinuous fringes cut by the bare ice area, around the fast-flowing ice stream areas as mentioned in Section 3.2. Therefore we connected phases from each outcropped area so that the unwrapped phases from the pixels on the coastline gave the same 0 m level phase. Then, trial-and-error adjustment of the SAR interferometry derived heights at the 23 GCP locations were done so that the SAR heights were consistent with the GCP heights in a least squares sense, by taking B_P as a parameter. The most probable B_P was obtained as 761 m, which indicated that the 2π phase change of the topographic fringe corresponded to a height change of 61 m. Although the B_P value of the three-pass interferogram (761 m) must be consistent with the difference (906 m) between that of the first interferogram (41 m) and that of the second interferogram (957 m), there remained a 145 m inconsistency because of inaccurate orbital parameters in the CEOS data sets.

Figure 5b illustrates the SAR interferometry derived DEM finally obtained by the above procedure. The generated DEM grids with a spatial resolution of 50 m by 50 m can express outcropped areas which are not shown on GTOPO30 contours in Fig. 5a, but

cannot contour the bare ice region and fast-flowing ice stream area because of weak co-registration of the SAR scenes. As shown in columns 6 and 7 of Table 1, SAR interferometry derived heights (column 6) are consistent with the GCP heights, showing zero-mean residuals and an rms error of 15.3 m for the residuals (column 7); this is one order of magnitude better than the similar comparison for GTOPO30.

6. Concluding Remarks

We obtained a DEM in the Sôya Coast area, Antarctica, by applying the three-pass interferometry method to JERS-1 SAR scenes. The obtained DEM is in much better agreement with the GCP heights, giving an rms error of 15.3 m, and features more detailed topographic undulations than GTOPO30. However, SAR interferometry derived DEM could not cover the bare ice areas nor fast-flowing ice stream areas.

More balanced installation of GPS-controlled GCPs on the ice sheet of higher elevation may reduce the rms error. Accurate phase unwrapping in the region with dense fringes and large discontinuities, and more accurate removal of orbital fringes, will also reduce the rms error of the derived DEM. The Advanced Land Observing Satellite (ALOS) which has an L-band SAR (Phased Array type L-band Synthetic Aperture Radar: PALSAR) will be launched in 2002 by NASDA (WAKABAYASHI *et al.*, 1998), and a precise orbit tracking system to assure one-meter accuracy of the orbit determination may reveal undetected features on the ice sheet and may provide much accurate DEM over the Antarctic ice sheet.

Acknowledgments

The authors are grateful to Dr. A. TANAKA of the Geological Survey of Japan, Prof. Y. FUJII of the National Institute of Polar Research (NIPR), Dr. Y. NOGI of NIPR and an anonymous reviewer for their careful reading of the manuscript and useful comments. The authors also thank JARE satellite receiving teams at Syowa Station, NASDA/EOC and RESTEC for providing us JERS-1 SAR data. The Ministry of International Trade and Industry (MITI) and NASDA retain ownership of the original JERS-1 data.

References

BRITISH ANTARCTIC SURVEY, SCOTT POLAR RESEARCH INSTITUTE and WORLD CONSERVATION MONITORING CENTRE (1993): Antarctic digital database user's guide and reference manual. Cambridge, SCAR, 156 p.

DIETRICH, R., DACH, R., KORTH, W., METZIG, R. and PERLT, J. (1997): Ice-ocean-solid earth interactions in Dronning Maud Land/Antarctica: A geodetic approach to solve open questions. Proc. IAG Symposia, Rio de Janeiro, **119**, 504–509.

DOI, K., OZAWA, T., SHIBUYA, K., NAKAGAWA, H., OMURA, M. and KOIKE, K. (1998): Preliminary study to generate a DEM of Amundsen Bay, Antarctica by interferometric SAR. Polar Geosci., **11**, 14–22.

GOLDSTEIN, R.M., ZEBKER, H.A. and WERNER, C.L. (1988): Two-dimensional phase unwrapping. Radio Sci., **4**, 713–720.

GOLDSTEIN, R.M., ENGELHARDT, H., KAMB, B. and FROLICH, R.M. (1993): Satellite radar interferometry for monitoring ice sheet motion: Application to an Antarctic ice stream. Science, **262**, 1525–1530.

GRAHAM, L.C. (1974): Synthetic interferometer radar for topographic mapping. Proc. IEEE, **62**, 763–768.

JOUGHIN, I., WINEBRENNER, D., FAHNESTOCK, M., KWOK, R. and KRABILL, W. (1996): Measurement of ice-sheet

topography using satellite-radar interferometry. J. Glaciol., **42**, 10–22.

KAMIYAMA, K., FURUKAWA, T., MAENO, H., KISHI, T. and KANAO, M. (1994): Glaciological data collected by the 33rd Japanese Antarctic Research Expedition in 1992. JARE Data Rep., **194** (Glaciology 21), 1–67.

KIMURA, H., NISHIO, F., YAMAGUCHI, Y., FURUKAWA, T., CHO, K. and WAKABAYASHI, H. (1999): Application of JERS-1 SAR interferometry. JERS-1 Science Program '99 PI Reports, ed. by JERS-1 Science Program Office, NASDA, EORC, 149–156.

KWOK, R. and FAHNESTOCK, M.A. (1996): Ice sheet motion and topography from radar interferometry. IEEE Trans. Geosci. Remote Sensing, **34**, 189–200.

LI, F.K. and GOLDSTEIN, R.M. (1990): Studies of multi-baseline spaceborne interferometric synthetic aperture radars. IEEE Trans. Geosci. Remote Sensing, **28**, 88–97.

MASSONET, D., ROSSI, M., CARMONA, C., ADRAGNA, F., PELTZER, G., FEIGL, K. and RABAUTE, T. (1993): The displacement field of the Landers Earthquake mapped by radar interferometry. Nature, **364**, 138–142.

MÜLLER, U., SIEVERS, J. and WALTER, H. (1997): SAR data exploitation for monitoring Antarctic ice sheets and glacier. Proc. 3rd ERS Symp., Florence, 877–880.

OOTAKI, O. and FUJIWARA, S. (1998): Measurement of ice sheet movement at S16, East Antarctica using GPS. Polar Geosci., **11**, 9–13.

RIGNOT, E. and MACAYEAL, D.R. (1998): Ice-shelf dynamics near the front of the Filchner-Ronne Ice Shelf, Antarctica, revealed by SAR interferometry. J. Glaciol., **44**, 405–418.

SHIBUYA, K. and ITO, K. (1983): On the flow velocity of the ice sheet along the traverse route from Syowa to Mizuho Stations, East Antarctica. Mem. Natl Inst. Polar Res., Spec. Issue, **28**, 260–276.

SHIBUYA, K., DOI, K. and AOKI, S. (1999): Precise determination of geoid height and free-air gravity anomaly at Syowa Station, Antarctica. Earth Planets Space, **51**, 159–168.

SHIMIZU, H., YOSHIMURA, A., NARUSE, R., WATANABE, O., NAKAWO, M. and OKUHIRA, F. (1975): Movement of ice sheet and glaciers in Sôya Coast in 1969–1972. JARE Data Rep., **27**, (Glaciology 2), 162–174.

TAKAHASHI, A., FUJII, Y., CHO, K., NISHIO, F., FURUKAWA, T. and WATANABE, O. (1995): Application of synthetic aperture radar (SAR) imagery on Antarctic glaciology. Nankyoku Shiryô (Antarct. Rec.), **39**, 205–232 (in Japanese with English abstract).

TOBITA, M., FUJIWARA, S., OZAWA, S., ROSEN, P.A., FIELDING, E.J., WERNER, C.L., MURAKAMI, M., NAKAGAWA, H., NITTA, K. and MURAKAMI, M. (1998): Deformation of the 1995 North Sakhalin Earthquake detected by JERS-1/SAR interferometry. Earth Planets Space, **50**, 313–325.

URAI, M. and YAMAGUCHI, Y. (1996): Application of differential synthetic aperture radar interferometry to the earth science: Potential for geothermal reservoir monitoring. Bull. Geol. Surv. Jpn., **47**, 23–31 (in Japanese with English abstract)

USGS (UNITED STATES GEOLOGICAL SURVEY) (1996): GTOPO30 documentation. Sioux Falls, SD, USA.

VEXCEL CORPORATION (1998): VEXCEL 3DSAR SAR Processing System Users Manual. Boulder, CO, USA, 120 p.

WAKABAYASHI, H., OSAWA, Y. and HAMAZAKI, T. (1998): PALSAR system on the ALOS. Proc. SPIE EurOPTO series, Barcelona, 181–189.

WESSEL, J.K. and SMITH, F. (1995): Free software helps map and display data. EOS; Trans., **72**, 445–446.

ZEBKER, H.A. and GOLDSTEIN R.M. (1986): Topographic mapping from interferometric synthetic aperture radar observations. J. Geophys. Res., **91**, 4993–4999.

(Received March 15, 1999; Revised manuscript accepted May 19, 1999)